

Polariton states bound to defects in GaAs/AlAs planar microcavities

Joanna M. Zajac* and Wolfgang Langbein

School of Physics and Astronomy, Cardiff University, The Parade, Cardiff CF24 3AA, United Kingdom

Maxime Hugues and Mark Hopkinson

Department of Electronic and Electrical Engineering, University of Sheffield, Mappin Street, Sheffield S1 4JD, United Kingdom

(Received 13 November 2011; published 12 April 2012)

We report on polariton states bound to defects in planar GaAs/AlAs microcavities grown by molecular beam epitaxy. The defect types relevant for the spatial polariton dynamics in these structures are cross-hatch misfit dislocations, and point-like defects extended over several micrometers. We attribute the latter defects to Ga droplets emitted occasionally by the Ga cell during the growth. These defects, also known as oval defects, result in a dome-like local modulation of surface, which is translated into the cavity structure and leads to a lateral modulation of the cavity polariton energy. The resulting spatially localized potential landscape for the in-plane polariton motion creates a series of bound states. These states were characterized by spectrally resolved transmission imaging in real and reciprocal space, and reveal the spatial potential created by the defects. Interestingly, the defect states exhibit long lifetimes between 10 and 100 ps, which we attribute to a spatially smooth confinement potential.

DOI: [10.1103/PhysRevB.85.165309](https://doi.org/10.1103/PhysRevB.85.165309)

PACS number(s): 78.67.Pt, 78.20.-e, 78.66.Fd

I. INTRODUCTION

Semiconductor microcavities have been extensively studied in last 20 years.^{1–3} Significant attention was given to planar microcavities, which are Fabry-Perot resonators, with a photon mode confined in growth direction by Bragg mirrors made of pairs of $\lambda/4$ layers of alternating refractive index. The in-plane dispersion of the cavity mode is close to quadratic for in-plane wave vectors k much smaller than the free-space wave vector, with a curvature described by an effective mass about 4 orders of magnitude smaller than the free electron mass. This implies a significant dispersion within the external optically accessible wave vector range. When coupled to a quantum well exciton, these microcavities show fundamental condensed-matter phenomena like strong coupling, Bose-Einstein condensation, lasing, parametric amplification. In many cases, these effects are significantly affected by the disorder in the structures. This leads to localization of the Bose-Einstein condensate, formation of vortices, and can be used as a probe for the dynamics of excitations of the polaritonic superfluid phase.^{4–6}

The three dimensional confinement of the cavity mode by artificial in-plane structures was investigated experimentally and theoretically in Refs. 7–11. In these works, circular mesas with diameters of 3–19 μm and heights in the nanometer range were created by lithography on the GaAs cavity layer before growing the top Bragg mirror (AlAs/GaAs).

In nominally planar GaAs based samples grown by molecular beam epitaxy (MBE) it is typically observed that the cavity mode is elastically scattered on a cross-hatched dislocation pattern,^{12–16} while the excitonic part tends to exhibit a more isotropic disorder on the relevant micrometer length scale. In samples grown by metal-organic chemical-vapor deposition (MOCVD), additional random disorder is observed, indicating a fluctuation of the layer thickness in the micrometer spatial range due to the growth mode influenced by transport of the reactants via the gas phase, allowing for nonhomogeneous deposition. In MBE instead, the molecular beam guarantees the random deposition of Ga atoms, and the surface diffusion,

which is limited to typically 100 nm, cannot create a long-range thickness modulation.

Apart from the cross-hatch dislocation pattern, one typically observes point-like defects (PD) with a surface density of about $10^4/\text{cm}^2$, which have a size and shape typical of those ascribed as oval defects.¹⁷ PDs are better visible in the regions of lower density of cross hatches, however were observed in all regions, and for different MC samples which we investigated until now. They are not related to strain relaxation, but are generally attributed to particle contamination during growth or Ga source spitting.¹⁸ These defects produce rather extended surface modulations, typically without lattice defects. Polariton modes in MCs have typical extensions of 10–100 μm , limited by mirror transmission or residual disorder. These modes are therefore sensitive to the length scale of the PDs, making an excellent probe for structural inhomogeneities in the 1–100 μm range. The resonant local transmission of the MC is modified by the PDs, creating spatially confined cavity modes, typically visible as a series of spectrally narrow localized modes, as will be shown here. The paper is organized as follows. In Sec. II the details of the samples and the experiment are given, followed by a description of the disorder inside these structures in Sec. III, and a presentation of the results of the optical measurements on localized states in Sec. IV. The origin of PDs is discussed in Sec. V.

II. SAMPLE AND EXPERIMENT

The sample investigated in this work is a bulk $1\lambda_c$ GaAs semiconductor microcavity (MC) surrounded by AlAs/GaAs distributed Bragg reflectors (DBRs) with 27 (24) $\lambda_c/4$ pairs on the bottom (top), respectively. The photon lifetime for this structure at zero in-plane wave vector calculated using the transfer matrix method is ~ 100 ps or $7\mu\text{eV}$, neglecting losses due to absorption and scattering by disorder. Images of the sample are shown in Fig. 1. At a temperature of $T = 80$ K, the cavity mode energy was $E_c = 1.485$ eV, red detuned by

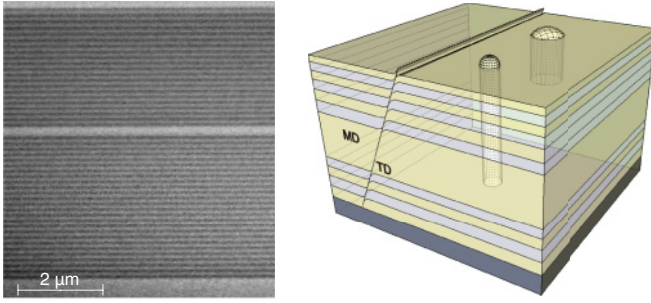


FIG. 1. (Color online) Scanning electron micrograph of the studied microcavity (left) and sketch of the sample structure (right) showing examples of defects, starting from different layers across the structure. MD and TD are examples of misfit and threading dislocations, respectively, which propagate across the structure.

23 meV from the bulk GaAs exciton in the cavity layer at 1.508 eV. The structure was grown in a VG V90 MBE machine with a hot-lip Veeco “SUMO” cell as Ga source. It was grown under continuous wafer rotation, resulting in a very weak ($<1\%$) thickness variation from the center to the edge of the wafer. The optical measurements of the polariton states were conducted at nitrogen temperature ($T = 80$ K) with the sample mounted strain-free in a bath cryostat. Real and reciprocal space transmission spectra were taken in the low-intensity regime. A sketch of the setup is shown in Fig. 2.

Two different optical excitation configurations were used. First, a single-mode external cavity diode laser (Sacher Lynx) with 5 MHz linewidth was employed to excite the polaritons at normal incidence ($\mathbf{k} = 0$) over a large size in real space (~ 1 mm) from the substrate side. This excitation allowed us to selectively image a specific polariton energy with a spectrally integrating detector. Secondly, a mode-locked Ti:sapphire laser (Coherent Mira) was used providing 100 fs pulses at 76 MHz repetition rate. The large spectral width of approximately 20 meV allows us to excite polariton bound states and the continuum dispersion simultaneously. The excitation was spatially focused to a spot of about $3 \mu\text{m}$ diameter using a lens of 0.15 numerical aperture, corresponding to an excitation wave vector range of $|\mathbf{k}| < 1.1/\mu\text{m}$. The emission was collected from the epi side by an aspheric lens of 0.5 NA (L3 in Fig. 2) with a wave vector range of $|\mathbf{k}| < 4/\mu\text{m}$, providing a spatial resolution of about $1 \mu\text{m}$. The emission was detected

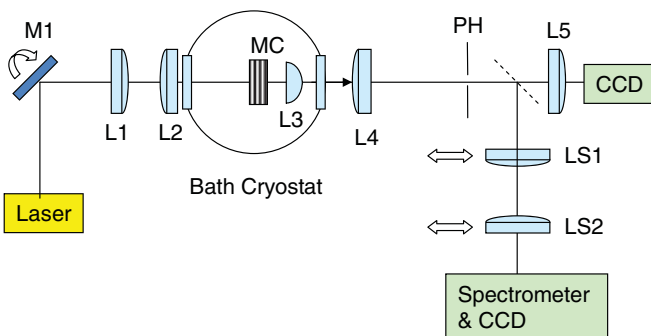


FIG. 2. (Color online) Sketch of the optical setup used to measure the localized polariton states. Both real space and reciprocal space imaging was used. L1–L5 Lenses, MC: microcavity sample, and LS1, LS2: moving lenses for imaging, for details see text.

spectrally integrated in the real or reciprocal space using video CCD cameras. For spectrally resolved detection, the emission was imaged in real or reciprocal space into the input slit of an imaging spectrometer. Two-dimensional images were acquired by translating the image across the spectrometer slit using lateral movements of two lenses (LS1 and LS2 in Fig. 2). Scans were made with $0.5 \mu\text{m}$ (real space) or $0.05 \mu\text{m}^{-1}$ (reciprocal space) steps.

III. DISORDER VARIATION VERSUS GROWTH TEMPERATURE

During the growth of the investigated structure, the temperature was ramped up to 715°C for the AlAs layers, and down to 660°C for the Bragg GaAs layers, and to 630°C for the GaAs cavity layer. For comparison, in Ref. 19 the sample was grown at a constant temperature of $620\text{--}630^\circ\text{C}$. A radial nonuniformity of the back-surface roughness due to As evaporation and resulting Ga-droplet formation was observed [see Fig. 3(g)]. This indicates that the growth temperature was

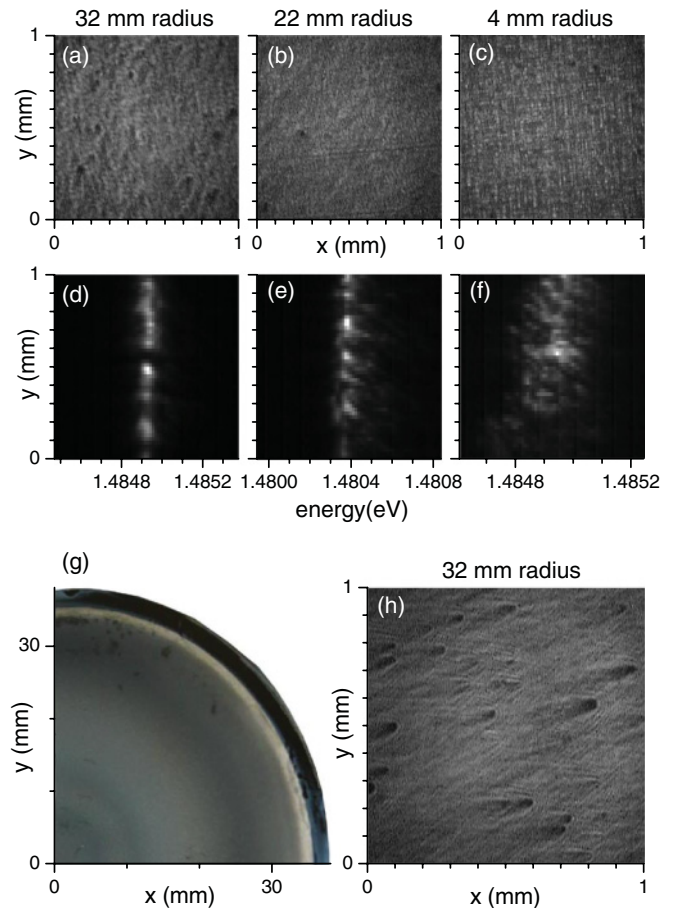


FIG. 3. (Color online) Disorder variation across the 3 in. wafer. Transmitted intensity for excitation at $\mathbf{k} = 0$ with 100 fs pulses resonant to the cavity mode for samples from different radial positions on the wafer as indicated. (a), (b), and (c) Spatially resolved, spectrally integrated. (d), (e), and (f) Spectrally resolved as function of y at a given x position. Linear gray scale from zero (black) to white. (g) Image of the back side of the wafer. (h) As (a) but for excitation at $\mathbf{k} \approx (-0.3, 0)/\mu\text{m}$.

nonuniform across the wafer, an effect which is significant due to the usage of an undoped and backside polished 3 in. wafer, leading to a weaker radiative coupling to the surrounding compared to doped wafers, increasing the infrared absorption, and unpolished wafers, decreasing the reflection, and avoiding radiation trapping by total-internal reflection. The cavity resonance energy was varying by only 0.5% over the wafer, indicating an exceptional flux homogeneity of the Ga and Al cells. The polariton disorder instead was found to vary significantly as function of radial position R on the wafer, as shown in Figs. 3(a)–3(f), where transmission images and spectra are shown at different R . Close to the center ($R = 4$ mm), a cross-hatch pattern is visible and the polariton states excited at $k = 0$ show an inhomogeneous broadening of ~ 100 μeV . This cross-hatch disorder decreases with increasing radius, and is not discernible at $R = 32$ mm close to the edge of the wafer. The cross-hatch pattern is due to the formation of a misfit-dislocation pattern found in (001) oriented strained cubic semiconductor thin film systems.²⁰ It is formed by strain relaxation via slides along the $\{111\}$ slip planes, which form lines along $[110]$ and $[1\bar{1}0]$ at their intersection with the film surface. Such a pattern is only observed for weakly strained films ($\epsilon < 2\%$), while for higher strains Stranski-Krastanov or Volmer-Weber growth is found. Cross-hatch patterns are typically reported for a lattice mismatch of the order of 1%, leading to a large density of slip lines and a significant surface modulation of several nanometers. The lattice mismatch of the GaAs/AlAs Bragg mirrors at room temperature²¹ is 0.14%. Using a mismatch of 0.07% of a Bragg period, we find a critical thickness for strain relaxation²² of about 2 μm . The Bragg mirrors have a total thickness of 6 μm , exceeding the critical thickness, and misfit dislocations form. However, the mismatch decreases with temperature,^{21,23} providing a lattice matched system at about 900 °C. We can therefore expect that the growth temperature influences the cross-hatch formation.

In the wafer region with low cross-hatch disorder ($R = 32$ mm) the inhomogeneous broadening of the polariton line is only about 30 μeV over millimeter sized regions. This exceptional spatial homogeneity is confirmed by the propagation of polaritons over hundreds of micrometers visible in Fig. 3(h), where the interference pattern of freely propagating polaritons with the ones scattered by the PDs is observed for oblique excitation a few degrees from normal corresponding to $\mathbf{k} \approx (-0.3, 0)/\mu\text{m}$. PDs are visible in all sample regions, and form natural defects which we investigate further in the subsequent sections.

The homogeneous polariton linewidth can be estimated by spectral speckle analysis²⁴ from the spectral speckle width in the spatially resolved transmission spectra shown in Figs. 3(d)–3(f), which are found to be similar to the spectrometer resolution. In the region $R = 32$ mm, spatial positions with a single peak transmission were present, which we fitted with a Voigt function. The full width at half maximum (FWHM) of Gaussian and Lorentzian parts of the spectrometer response, which are equal to 18 μeV each, were subtracted from the fitted broadenings of the measured line shapes. The deduced homogenous (Lorentzian) FWHM linewidths Γ were between 10 and 20 μeV , corresponding to lifetimes $T_1 = \hbar/\Gamma$ of 30–55 ps.

IV. POLARITON STATES BOUND TO POINT-LIKE DEFECTS

The spatial distribution of polariton energies can be visualized by resonant excitation with a spectrally narrow source. We used a single-mode external cavity diode laser (Sacher Lynx) with 5 MHz linewidth to excite the polaritons at normal incidence ($\mathbf{k} = 0$) over a large size in real space (~ 1 mm) from the substrate side. The emission from the epi side was imaged onto a CCD. By tuning the excitation photon energy below the band edge of the extended cavity polaritons, individual localized states can be excited resonantly and appear as bright spots. By scanning the photon energy, the localized defect states within the excited area are sequentially addressed according to their eigenenergy. An example is shown in Fig. 4, where images corresponding to three different excitation photon energies are overlaid into a color image. The different colors of the localized states show their different eigenenergies $\hbar\omega_n$. Different shapes of the localized states are also visible, and we find an average distance of a few 10 μm of the PDs with localized states separated by more than 1 meV from the band edge.

To gain more detailed information about the set of states bound to an individual PD, we change excitation and detection setup to the pulsed 100 fs source centered ~ 10 meV below the polariton band edge, spatially focused onto the PD. The emission was measured using spectrally resolved imaging in either real or reciprocal space, as discussed in Sec. II. The resulting data for the polariton states bound to PD 1 are shown in Fig. 5. On the left the directionally and spectrally resolved intensity $I(k_x = 0, k_y, \omega)$ is given on a logarithmic scale showing bound resonances and the continuum. A series of $n_1 = 16$ discrete resonances is discernible, at frequencies ω_n , $n = 1, \dots, n_1$. The intensity distributions at these resonances in real and reciprocal space, $I(x, y, \omega_n)$ and $I(k_x, k_y, \omega_n)$, respectively, are proportional to the probability distributions $|\Psi_n|^2$ of the corresponding state wave functions Ψ_n (assuming that the Bragg mirror reflectivity is independent of \mathbf{k} and all relevant emission directions \mathbf{k} are imaged). For convenience

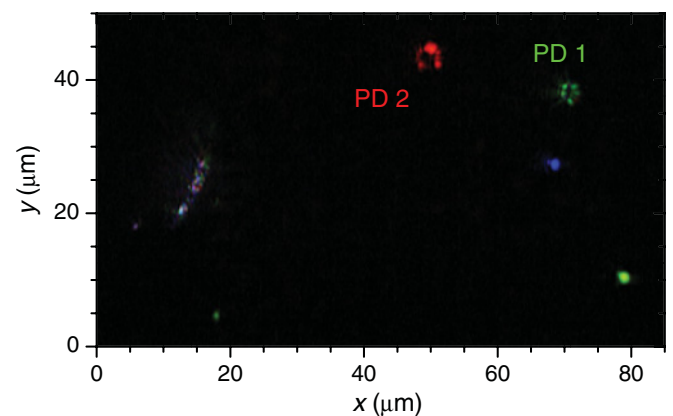


FIG. 4. (Color online) Spatially resolved color coded transmission intensity for photon energies of 1482.1 meV (blue channel), 1482 meV (magenta channel), and 1473.8 meV (yellow channel). Two localized states are labeled PD 1 and PD 2 for later reference. Animations of the data over the photon energy are available in Ref. 25.

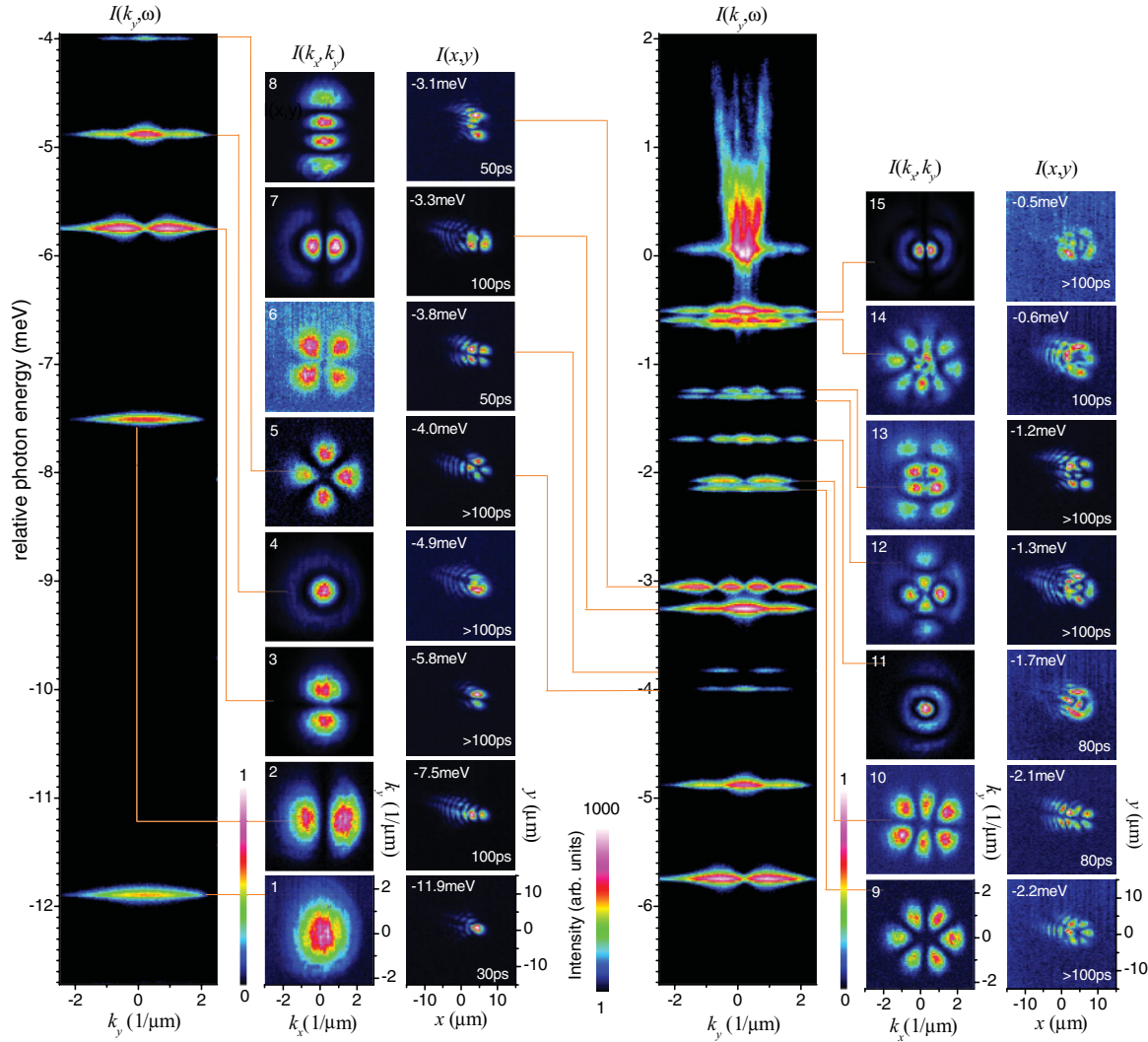


FIG. 5. (Color online) Spectral imaging of the emission from polariton states close to PD 1 of Fig. 4 in real and reciprocal space. The figure is split into two columns for space reasons. Each column shows on the left the intensity $I(k_x = 0, k_y, \omega)$ on a logarithmic color scale as indicated. The energy $\hbar\omega$ is shown relative to the polariton band edge at $\hbar\omega_c = 1.4833$ eV. The intensity of the individual states is given in the middle in reciprocal space $I(k_x, k_y, \omega_n)$, and on the right in real space $I(x, y, \omega_n)$, using a linear color scale normalized to the maximum for each state. The state number, the resonance energies relative to the band edge $\hbar\omega_n - \hbar\omega_c$ and the lifetimes, are shown for each state. The connection lines indicate the corresponding state in $I(k_x = 0, k_y, \omega)$. The tails visible in $I(x, y, \omega_n)$ are due to imaging aberrations relevant at large \mathbf{k} .

we show the localization energy $\Delta_n = \hbar\omega_n - \hbar\omega_c$ of the states, where $\hbar\omega_c$ is the band edge given by the minimum of the parabolic dispersion of free polaritons. The lifetime of each state is also shown, deduced from the linewidth by correcting for the spectrometer response, using a Voigt-fit as described in Sec. III. From the systematic error in the fit we estimate an error of $5 \mu\text{eV}$ in the deduced linewidths, limiting the maximum measurable lifetime to about 100 ps. Many of the states show lifetimes in the order of 100 ps, corresponding to a Q factor of 4×10^5 , one order of magnitude higher than measured in microcavity mesa structures reported in Ref. 7.

In Fig. 5 the ground state Ψ_1 is observed at $\Delta_1 = -11.9$ meV. The shapes of the wave functions reveal a nearly cylindrical symmetry of the effective confinement potential

$V_1(x, y)$ created by PD 1. The first excited state Ψ_2 is found at $\Delta_2 = -7.6$ meV, and shows a p_x -like symmetry, with a node at $x = 0$. Ψ_3 has $\Delta_3 = -5.8$ meV and a p_y -like symmetry with a node at $y = 0$. The energy splitting of $\Psi_{2,3}$ shows a breaking of cylindrical symmetry of $V_1(x, y)$. The next three states correspond to d states, Ψ_4 having zero angular momentum and two nodes in radial direction, and $\Psi_{5,6}$ being superpositions of angular momentum 2. The nondegeneracy of the different $n = 2$ states shows the nonparabolicity of the confinement. The higher states can be classified in a similar way with increasing number of nodes in the wave function.

PD 2 instead is not cylindrically symmetric as shown in Fig. 6. The two lowest states $\Psi_{1,2}$ are separately localized to the left and the right of the defect center with an s -like wave function, indicating two separate minima of the potential. The

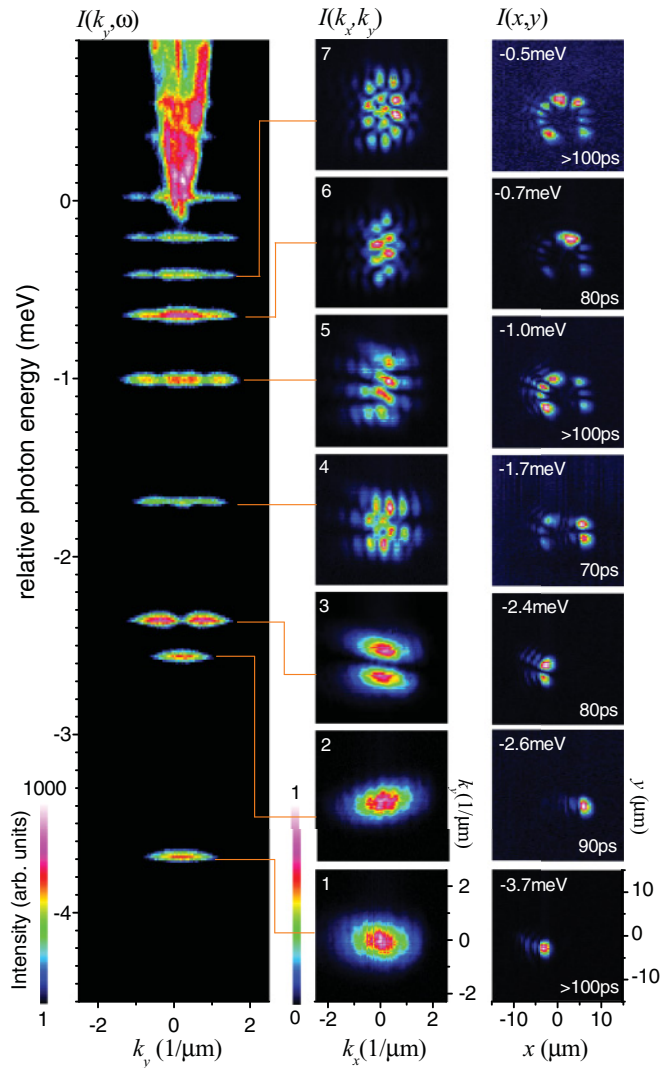


FIG. 6. (Color online) As Fig. 5, but for PD 2 of Fig. 4 and $\hbar\omega_c = 1.4826$ eV.

left minimum confines also a p -like excited state Ψ_3 , while the corresponding excited state on the right Ψ_4 is already extended along a horseshoe-shaped region, coupling to a d -like state of the left minimum. The next state Ψ_5 is a mixture of the left f -like state with the right d -like state. Ψ_6 is mostly localized on the tip of the horseshoe, possibly due to a local potential maximum close to the state energy, which is supported by the relatively small wave vector spread in k_x . A total of $n_3 = 11$ states are visible. Some resonances are observed even above the continuum, indicating the presence of a potential barrier between the defect region and the surrounding continuum. These states could lead to resonant scattering similar to Feshbach resonances observed in atomic physics.

The last reported defect PD 3 (see in Fig. 7, not shown in Fig. 4) is similar to PD 1 in being approximately circular symmetric, but about a factor of 3 shallower. The ground state Ψ_1 is s -like, and shows a larger extension in real space and a smaller in reciprocal space than the ground state of PD1, as expected from the weaker confinement. A total of $n_3 = 11$ states are visible.

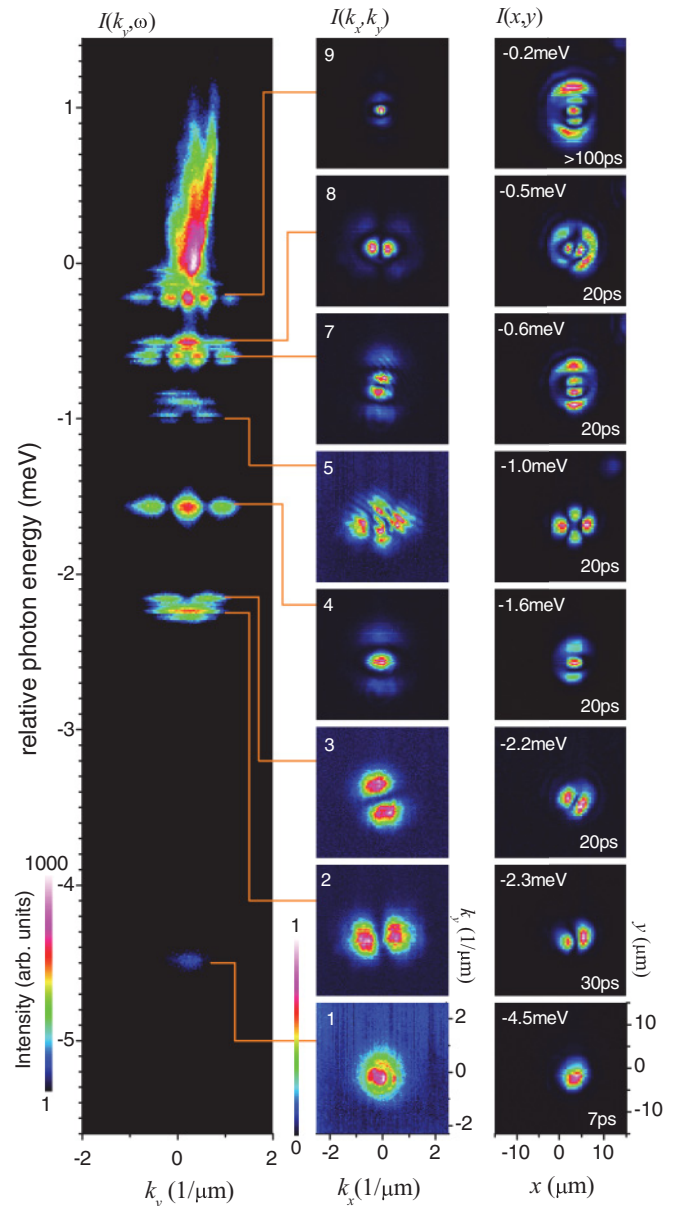


FIG. 7. (Color online) As Fig. 5 but for PD 3 (not shown on Fig. 4), and $\hbar\omega_c = 1.4815$ eV.

A. Coherent wave packet dynamics

In the transmission experiment, all states are excited simultaneously and coherently to each other by the focused femtosecond laser pulse as was discussed in Sec. II. The resulting transmission is accordingly a coherent superposition of the emission by the states after excitation. As seen in Fig. 7, some states have a small energy difference, comparable to their linewidth. The emission at an energy close to their eigenenergy is thus a coherent superposition of the states, with an initial phase and amplitude determined by the spatial overlap between the state and the excitation field. We illustrate the effect of such a coherent superposition here with two examples.

First, we note the two p -like excited states $\Psi_{2,3}$ of PD 3 which are nearly degenerate (≈ 100 μ eV separation). The emitted field close to their energy is a coherent superposition of the two wave functions $a\Psi_2 + b\Psi_3$, with amplitudes determined

by the excitation. To compare the measurements with the theoretically expected result, we assume harmonic confinement and p -like wave functions $\Psi_{2,3} \propto (k_x, k_y) \exp(-\frac{k_x^2 + k_y^2}{a^2})$ with frequencies $\omega_{2,3}$ and linewidths $\gamma_{2,3}$ which are a sum of the state linewidth and spectrometer resolution. The measured wave function can be modeled as a coherent superposition of the two near-resonant states with a relative phase ϕ and amplitude η given by the excitation conditions. This superposition can be written as

$$\Psi(\mathbf{k}, \omega) \propto \left(\frac{k_x}{\omega - \omega_2 + i\gamma_2} + \eta e^{i\phi} \frac{k_y}{\omega - \omega_3 + i\gamma_3} \right) e^{-\frac{k_x^2 + k_y^2}{a^2}}. \quad (1)$$

Similarly, for the d -like $l = 2$ states $\Psi_{5,6} = (k_x k_y, k_x^2 - k_y^2) \exp(-\frac{k_x^2 + k_y^2}{a^2})$ with frequencies $\omega_{5,6}$ and linewidths $\gamma_{5,6}$,

$$\Psi(\mathbf{k}, \omega) \propto \left(\frac{k_x k_y}{\omega - \omega_5 + i\gamma_5} + \eta e^{i\phi} \frac{k_x^2 - k_y^2}{\omega - \omega_6 + i\gamma_6} \right) e^{-\frac{k_x^2 + k_y^2}{a^2}}. \quad (2)$$

Simulations according to these wave functions, using parameters values taken from the experiment as indicated in Fig. 8, give a qualitative agreement with measurements. Animations of the data over the photon energy are available in Ref. [25].

B. Confining potential

The observed localized polariton states can be related to an effective confinement potential $V_m(\mathbf{r})$ for the in-plane polariton motion. We can estimate $V_m(\mathbf{r})$ using the spectrally integrated density of states $D_m(\mathbf{r})$ created by $V_m(\mathbf{r})$ below the continuum edge in the following way. On the one hand, this density can be calculated from the spatially resolved bound density of states

$$D_m(\mathbf{r}) = \sum_{n=1}^{n_m} |\Psi_n(\mathbf{r})|^2, \quad (3)$$

where the bound state probability densities $|\Psi_n(\mathbf{r})|^2$ are taken as the normalized measured intensity

$$|\Psi_n(\mathbf{r})|^2 = \frac{I(\mathbf{r}, \omega_n)}{\int I(\mathbf{r}, \omega_n) d\mathbf{r}^2}. \quad (4)$$

This expression assumes that the emitted field is proportional to the polariton wave function, which is valid for a cavity lifetime, which is constant for the in-plane wave vector components of the bound states. This is a good approximation for the data shown here since the maximum in-plane wave vector of about $2/\mu\text{m}$ is only 8% of the light wave vector in the Bragg mirrors.

On the other hand, $D_m(\mathbf{r})$ is given by the integral of the free density of states from zero kinetic energy at the potential floor to the continuum when neglecting the spatial variation of the confinement potential, that is, in the limit of small level splitting compared to the confinement potential. In two dimensions the density of states is constant and given by $D_{2D} = m/(2\pi\hbar^2)$, such that the integral over the density

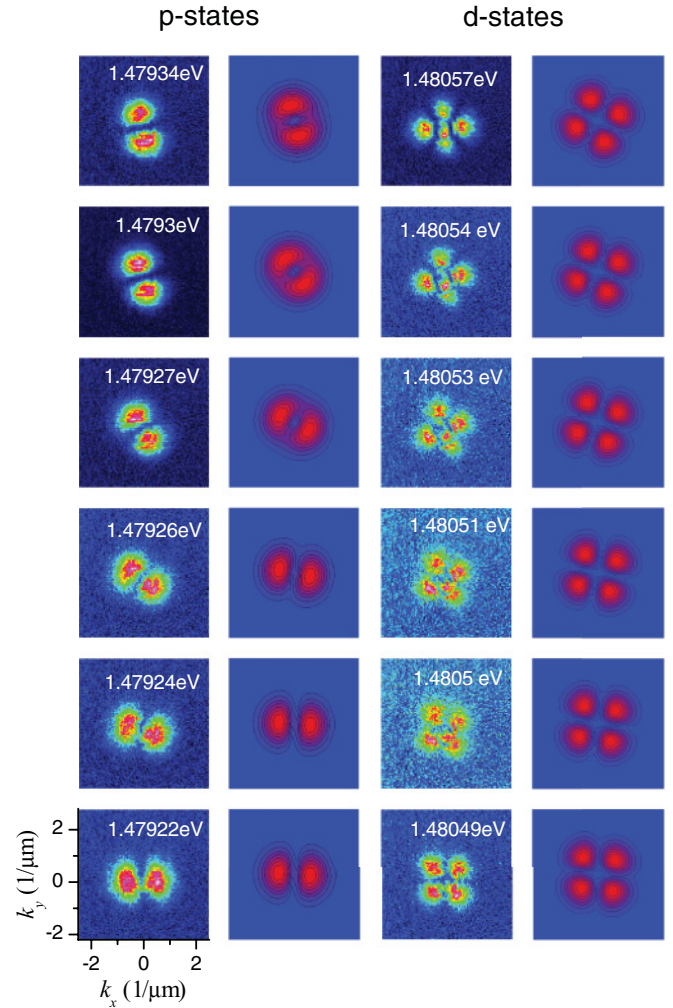


FIG. 8. (Color online) Measured intensities $I(\mathbf{k}, \omega)$ from the same experiment as shown in Fig. 7 for energies $\hbar\omega$ as labeled, using fine steps across the p -states (left) and d -state (right) resonances. The corresponding simulated $|\Psi(\mathbf{k}, \omega)|^2$ for the same energies are given to the right of each experimental intensity image. The energy is given in the upper part of each image, and increases from lower to upper panels as labeled. The parameters used in simulations according to Eqs. (1) and (2) were $\hbar\omega_2 = 1.479115$ eV, $\hbar\omega_3 = 1.479295$ eV, $\hbar\gamma_2 = 58$ μeV , $\hbar\gamma_3 = 73$ μeV , $\eta = 1$, $\phi = 0$ for the p -state simulation, and $\hbar\omega_5 = 1.480381$ eV, $\hbar\omega_6 = 1.480559$ eV, $\hbar\gamma_5 = 37$ μeV , $\hbar\gamma_6 = 50$ μeV , $\eta = 1$, $\phi = 0$ for the d -state simulation.

of states is given by $-V_m(\mathbf{r})D_{2D}$, and we find $V_m(\mathbf{r}) = -D(\mathbf{r})/D_{2D}$. We use the effective mass of the polaritons from the measured dispersion $m = 2 \times 10^{-5} m_e$, where m_e is the free electron mass. The resulting confinement potentials for the three investigated PDs are shown in Fig. 9. The symmetry of the potentials reflect the symmetry of the localized states. Comparing with the energies of the confined states, $V_m(\mathbf{r})$ seems about factor of 2 too small. Errors in the scaling of $V_m(\mathbf{r})$ are due to the length calibration of the imaging, which we estimate to have an accuracy of 30%, yielding a 70% error in $V_m(\mathbf{r})$, and to the effective mass m which we estimate to have an error of 10%. Furthermore, the approximation of a small level splitting compared to the confinement potential yields an error intrinsic to the model. Using numerical simulations for

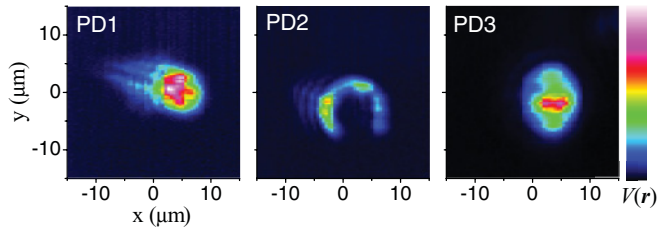


FIG. 9. (Color online) Confinement potential $V_m(\mathbf{r})$ estimated from the bound density of states $D_m(\mathbf{r})$ for the three PDs, on a color scale as given from 0 (black) to -5.4 meV (white).

a square well potential we find that the finite number of levels n_m leads mostly to spurious spatial oscillations in the predicted potential, while the average is reproduced to a relative error of $1/n_m$, so about 10%–20% in our case. A direct comparison of the polariton states and their energies in the confining potential $V_m(\mathbf{r})$ could be used to determine the $V_m(\mathbf{r})$ more accurately.

V. ORIGIN OF THE POINT-LIKE DEFECTS

The formation of the PDs could be due to a variety of different physical processes. Among them, there are threading dislocations (TD), either propagating from the substrate or created in the epilayers due to surface defects. Usually by growing multilayer structures threading dislocations from the substrate are suppressed as they bend on GaAs/AlAs interfaces and propagate parallel to the $\langle 110 \rangle$ directions suppressing the dislocation density even to 5% of its original value.²⁶ The investigated sample was grown on a wafer with a TD density of about $2 \times 10^3/\text{cm}^2$ specified by the manufacturer, which is comparable to the observed defect density.

In order to investigate if the observed PDs are related to threading dislocations, we used an etching procedure^{27,28} for $\{100\}$ GaAs crystal facets, which requires less equipment and sample preparation as compared to the alternative method of transmission electron microscopy. It also allows us to investigate large surface areas, which is necessary considering the small defect density, and provides a one-to-one correspondence between etched pits and threading dislocations. Since the sample is not destroyed in the process, it is possible to spatially correlate the etched pits corresponding to the threading dislocations with the PDs. The etching method reveals the dislocations by enhanced material removal around the dislocation core. Prior to etching, the sample surface is cleaned by successively immersing in trichloroethane, acetone, methanol, and isopropanol at 80°C for 5 min, followed by a dip in deoxidizing 5% solution of ammonia in water at room temperature for 30 s. The resulting surface was assessed using an optical microscope and SEM. The KOH etchant was prepared from granules which were melted in a test tube under an open flame, and then placed on a hotplate at 360°C . The sample was immersed into the molten KOH for 2 min. The resulting etch pits on the sample surface were observed in a reflective DIC (differential interference contrast) optical microscope. We found an etch-pit density of about $10^3/\text{cm}^2$, consistent with the manufacturer specification of the threading dislocations density for the GaAs wafer used as a substrate. An overview of several defects obtained using DIC microscopy is shown in Fig. 10. Each rectangular etch pit marks a threading

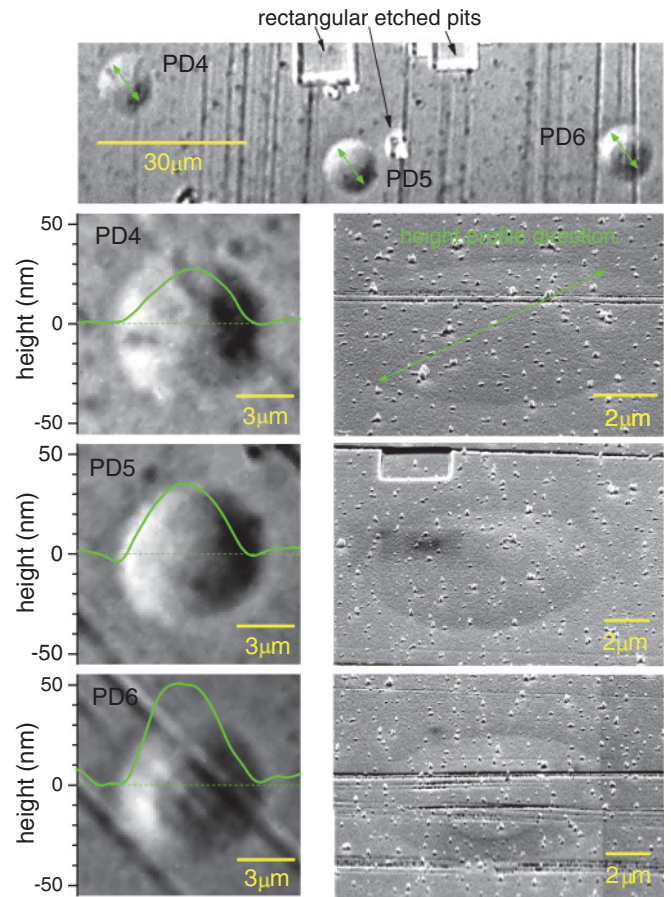


FIG. 10. (Color online) Top: Sample surface after KOH etching imaged with DIC. Round defects corresponding to PDs are labeled. Below on the left column, individual height profiles of PDs obtained using DIC with the corresponding DIC images. In the right column, corresponding FESEM images of the PDs taken at grazing incidence of 70° to the surface normal. The vertical scale is stretched for clarity. The grains on the surface are due to post-growth contamination.

dislocation in its center. The lines are scratches on the sample surface and/or misfit dislocations.

Subsequently, low temperature transmission measurements were repeated together with reflection microscopy. The positions of the PDs were found to be not correlated to the etch pits. Instead, the PDs coincide with the round to oval structures of 7–10 μm diameter on the sample surface, as observed in Fig. 10. These defects are thus the origin of the localization potentials for the polaritons.

From the DIC images we have quantitatively extracted the surface profile of the PDs. They show a typical surface height modulation of several tens of nanometers, being approximately parabolic with a small depression about 10% of the height below the original surface at the edge, and a width of a few micrometers. The energy barrier to the continuum observed in the localized states (see Sec. IV) is likely to be related to this edge depression.

Also atomic force microscopy images of the surface were obtained, but due to the large extension and small height of the PDs, no reliable results of the large scale topography could be extracted.

Using field emission scanning electron microscopy (FESEM), the structures were imaged under grazing angle of incidence (70° to the surface normal) to enhance the contrast for the flat surface topography, and results are shown in Fig. 10. The shape is consistent with the DIC images. A ridge shaped structure close to the center of the dome is also visible.

Growth related defects were categorized in Ref. 18, showing some defects which qualitatively resemble the ones discussed here. We observed defects with different shapes, with the most common being nearly round defects with a weak ridge in the center, as shown in Fig. 10. According to Ref. 18 round defects with nucleus originate from Ga oxide or spitting, while obscure ovals arise from Ga droplets, oxides, or particle contaminants. We attribute the observed defects to Ga nanodroplets emitted by the Ga cell during growth. Once deposited on the surface, the Ga is converted to GaAs, forming a hill with a depression in the center due to the growth kinetics. During the subsequent growth, lateral Ga diffusion leads to an extension of the hill while its height is reduced. Interestingly, we observe nearly round defects in the present sample, while on similar samples grown throughout at a lower temperature of 630°C similar defects are observed, which are elliptical with an about 1 : 3 ratio of extension in the $[110]$ to $[1\bar{1}0]$ directions. We attribute this observation to the temperature-dependent anisotropic Ga mobility on the surface.

Clearly the impact of such a structure on the polaritons depends on the position of the Ga droplet deposition within the MC structure in growth direction. This information is not accessible in the characterization techniques reported here, which are all measuring the surface topography of the structure. To investigate this further, we used combined focused ion beam (FIB)–scanning electron beam (SEM) to cut with FIB into the structure and measure the exposed sidewall by SEM.²⁹ By sequentially slicing the structure,

volume information on the defect is obtained. The results of this investigation including a study on the influence of the droplet positions relative to the cavity layer on polariton confinement will be reported in a forthcoming work.

VI. SUMMARY

In summary, we have identified point-like defects in planar microcavities which lead to series of spectrally sharp localized polariton states. The localized polariton states were characterized in real and reciprocal space and the underlying confinement potential has been reconstructed from these measurements. The symmetry of the states can be close to cylindrical. The origin of the defects is attributed to spitting of the Ga cell during MBE growth, depositing Ga droplets of a size in the order of 100 nm onto the sample surface during growth. Due to the large thickness of microcavity structures, the surface density of these droplets is enhanced, and the spatially extended polariton states are exceptionally sensitive to the resulting extended structural variations. The induced confinement potential can be rather smooth, allowing for confined states of small linewidth since the scattering into the lossy microcavity modes at high wave vectors is suppressed.

ACKNOWLEDGMENTS

We thank A. Drevisi and I. Fallis for assistance with the KOH etching. This work was supported by the EPSRC UK Research Council (Grant No. EP/F027958/1). Author contributions: W.L. designed the samples, M.H. and M.H. grew the samples at the EPSRC National Centre for III-V Technologies, Sheffield, UK, and gave feedback on sample design, J.Z. performed the structural measurements, J.Z. and W.L. performed the optical measurements, analyzed the data, and prepared the manuscript.

*ZajacJM@cardiff.ac.uk

¹A. Kavokin, J. J. Baumberg, G. Malpuech, and F. P. Laussy, *Microcavities* (Oxford University Press, Oxford, 2007).

²A. Q. B. Deveaud-Plédran and P. Schwendimann, eds., *Quantum Coherence in Solid State Systems*, Vol. 171 of International School of Physics Enrico Fermi (IOS Press, New York, 2009).

³M. S. Skolnick, T. A. Fisher, and D. M. Whittaker, *Semicond. Sci. Technol.* **13**, 645 (1998).

⁴J. Kasprzak, M. Richard, S. Kundermann, A. Baas, P. Jeambrun, J. Keeling, F. Marchetti, M. H. Szymańska, R. André, J. Staehli *et al.*, *Nature (London)* **443**, 409 (2006).

⁵K. G. Lagoudakis, M. Wouters, M. Richard, A. Baas, I. Carusotto, R. André, D. L. S. Dang, and B. Deveaud-Plédran, *Nat. Phys.* **4**, 706 (2008).

⁶A. Amo, J. Lefrère, S. Pigeon, C. Adrados, C. Ciuti, I. Carusotto, R. Houdré, E. Giacobino, and A. Bramati, *Nat. Phys.* **5**, 805 (2009).

⁷R. I. Kaitouni, O. E. Daïf, A. Baas, M. Richard, T. Paraiso, P. Lugan, T. Guillet, F. Morier-Genoud, J. D. Ganière, J. L. Staehli *et al.*, *Phys. Rev. B* **74**, 155311 (2006).

⁸P. Lugan, D. Sarchi, and V. Savona, *Phys. Status Solidi C* **3**, 2428 (2006).

⁹R. Cerna, D. Sarchi, T. K. Paraiso, G. Nardin, Y. Lèger, M. Richard, B. Pietka, O. E. Daif, F. Morier-Genoud, V. Savona *et al.*, *Phys. Rev. B* **80**, 121309(R) (2009).

¹⁰R. Cerna, T. K. Paraiso, Y. Lèger, M. Wouters, F. Morier-Genoud, M. T. Portella-Oberli, and B. Deveaud-Plédran, *Phys. Rev. B* **81**, 113306 (2010).

¹¹G. Nardin, Y. Lèger, B. Pietka, F. Morier-Genoud, and B. Deveaud-Plédran, *Phys. Rev. B* **82**, 045304 (2010).

¹²M. Gurioli, F. Bogani, D. S. Wiersma, P. Roussignol, G. Cassaboïs, G. Khitrova, and H. Gibbs, *Phys. Rev. B* **64**, 165309 (2001).

¹³W. Langbein and J. M. Hvam, *Phys. Rev. Lett.* **88**, 047401 (2002).

¹⁴W. Langbein, in Proceedings of the 26th International Conference on the Physics of Semiconductors (2002).

¹⁵W. Langbein, *J. Phys.: Condens. Matter* **16**, S3645 (2004).

¹⁶W. Langbein, *Riv. Nuovo Cimento* **33**, 255 (2010).

¹⁷M. Herman and H. Sitter, *Molecular Beam Epitaxy* (Springer, Berlin, 1989).

¹⁸H. Kawada, S. Shirayone, and K. Takahashi, *J. Cryst. Growth* **128**, 550 (1993).

- ¹⁹U. Oesterle, R. P. Stanley, and R. Houdré, *Phys. Status Solidi B* **242**, 2157 (2005).
- ²⁰A. M. Andrews, J. S. Specka, A. E. Romanov, M. Bobeth, and W. Pompe, *J. Appl. Phys.* **91**, 1933 (2002).
- ²¹S. Adachi, *Properties of Aluminium Gallium Arsenide* (INSPEC, London, 1988).
- ²²J. W. Matthews and A. E. Blakeslee, *J. Cryst. Growth* **27**, 118 (1974).
- ²³M. Ettenberg and R. Paff, *J. Appl. Phys.* **41**, 3926 (1970).
- ²⁴G. Kocherscheidt, W. Langbein, G. Mannarini, and R. Zimmermann, *Phys. Rev. B* **66**, 161314(R) (2002).
- ²⁵See Supplemental Material at <http://link.aps.org/supplemental/10.1103/PhysRevB.85.165309> for animations of the data.
- ²⁶M. Shinohara, T. Ito, and Y. Imamura, *J. Appl. Phys.* **58**, 3449 (1985).
- ²⁷J. G. Grabmaier and C. B. Watson, *Phys. Status Solidi B* **32**, K13 (1969).
- ²⁸K. Bacher and J. J. S. Harris, *J. Electrochem. Soc.* **142**, 2386 (1995).
- ²⁹L. A. Giannuzzi and F. A. Stevie, eds., *Introduction to Focused Ion Beams: Instrumentation, Theory, Techniques, and Practise* (Springer, Berlin, 2005).